

VLEIBot: A New 45-mg Swimming Microrobot Driven by a Bioinspired Anguilliform Propulsor

Elijah K. Blankenship, Conor K. Trygstad, Francisco M. F. R. Gonçalves, and Néstor O. Pérez-Arancibia

Abstract—This paper presents the VLEIBot* (*Very Little Eel-Inspired roBot*), a 45-mg/23-mm³ microrobotic swimmer that is propelled by a bioinspired anguilliform propulsor. The propulsor is excited by a single 6-mg *high-work-density* (HWD) microactuator and undulates periodically due to wave propagation phenomena generated by *fluid-structure interaction* (FSI) during swimming. The microactuator is composed of a carbon-fiber beam, which functions as a leaf spring, and *shape-memory alloy* (SMA) wires, which deform cyclically when excited periodically using Joule heating. The VLEIBot can swim at speeds as high as 15.1 mm · s⁻¹ (0.33 Bl · s⁻¹) when driven with a heuristically-optimized propulsor. To improve maneuverability, we evolved the VLEIBot design into the 90-mg/47-mm³ VLEIBot⁺, which is driven by two propulsors and fully controllable in the *two-dimensional* (2D) space. The VLEIBot⁺ can swim at speeds as high as 16.1 mm · s⁻¹ (0.35 Bl · s⁻¹), when driven with heuristically-optimized propulsors, and achieves turning rates as high as 0.28 rad · s⁻¹, when tracking path references. The measured *root-mean-square* (RMS) values of the tracking errors are as low as 4 mm.

I. INTRODUCTION

The recent development of extremely light (1 to 10 mg) and small (0.45 to 1.89 mm³) fast (up to 40 Hz) actuators based on *shape-memory alloy* (SMA) technology enabled the creation of new types of microrobots, which can operate at low voltages and with simple excitation electronics [1]–[3]. These advancements predict that the vision of creating swarms and schools of insect-scale robots capable of performing essential tasks for humans will become a reality soon. Here, we present two new microrobotic surface swimmers, whose propulsion mechanism is inspired by the anguilliform swimming mode at a moderate ($\sim 10^2$ to $\sim 10^4$) *Reynolds number* (Re). These microrobots, shown in Fig. 1, are: (i) the VLEIBot, which weighs 45 mg, operates at frequencies up to 20 Hz, and achieves speeds as high as 15.1 mm · s⁻¹ (0.33 Bl · s⁻¹); and, (ii) the VLEIBot⁺, which weighs 90 mg, operates at frequencies up to 10 Hz, and achieves speeds as high as 16.1 mm · s⁻¹ (0.35 Bl · s⁻¹). Additionally, because of its dual propulsion mechanism, the VLEIBot⁺ is fully controllable in the *two-dimensional* (2D) space. We envision that in coordination with other flying and crawling insect-scale robots—advanced evolutions of those in [1]–[18]—teams of VLEIBot-type microswimmers will

This work was partially funded by the Washington State University (WSU) Foundation and the Palouse Club through a Cougar Cage Award to N. O. Pérez-Arancibia. Additional funding was provided by the WSU Voiland College of Engineering and Architecture through a start-up fund to N. O. Pérez-Arancibia.

E. K. Blankenship and C. K. Trygstad contributed equally to this work.

The authors are with the School of Mechanical and Materials Engineering, Washington State University (WSU), Pullman, WA 99164, USA. Corresponding authors' e-mail: conor.trygstad@wsu.edu (C. K. T.); n.perezarancibia@wsu.edu (N. O. P.-A.).

*We pronounce this word as *vl-ahy-bot*, thus producing the same sound in the pronunciations of *eigenvalue* and *Einstein*.

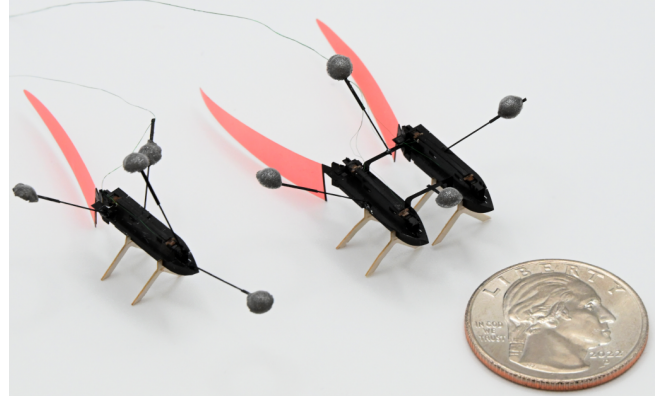


Fig. 1. **Photograph of the VLEIBot and VLEIBot⁺.** The VLEIBot (left) is a 45-mg swimming microrobot driven by a new bioinspired propulsor. The VLEIBot⁺ (right) is a 90-mg controllable microrobotic swimmer designed to achieve high maneuverability in the *two-dimensional* (2D) space.

assist humans in aquatic search and rescue missions, inspection of vessels and marine infrastructure, hydroponic agriculture, aquaculture tasks, research of shallow-water reefs, and minimally-invasive continuous automatic monitoring of water quality in reservoirs, just to mention a few.

The VLEIBot design exploits the surface tension of water to stay afloat and the *fluid-structure interaction* (FSI) of a flexible thin undulating tail with water to propel itself forward. In this case, the propulsor is driven by the 6-mg *high-work-density* (HWD) SMA-based actuator introduced in [1] and its design was loosely inspired by the anguilliform swimming mode exhibited by European eels (*Anguilla anguilla* L.) [19], yellow-bellied sea snakes (*Pelamis platurus*) [20], and young *African clawed frog* (ACF) tadpoles (*Xenopus laevis*) [21]. Anguilliform swimming is believed to be generated by sub-ambient pressure zones in the troughs of the swimmer's body waves and, for this reason, highly efficient regarding cost of transport. This is an FSI phenomenon observed at moderate Res ($\sim 10^2$ to $\sim 10^4$) [22], [23]. Given that the Res associated with the motion of the VLEIBot's propulsor are in the moderate range ($\sim 10^{-1}$ to $\sim 10^3$), we hypothesize that the same hydrodynamic effect occurs in this case and we considered it during the design process. In the past, researchers have distributively embedded SMA wires in semi-rigid bodies to generate undulation [24]–[29]; however, to our best knowledge, the VLEIBot's design is the first with onboard actuation that removes the need for complex propulsor configurations and fully exploits FSI phenomena to generate a wave that propagates along the swimmer's tail, thus producing locomotion. This is the key design element that enables anguilliform-inspired swimming at the mm-to-cm scale for the first time.

The most common actuation methods used to drive swim-

ming microrobots are based on electromagnetic [30]–[48], piezoelectric [49]–[55], and ionic-polymer [56]–[58] technologies. While electromagnetic actuation has enabled the functionality of very small and fast swimmers, some of which can operate inside the human body, this approach does not represent a path to full autonomy at the mm-to-cm scale because it requires the generation of large external magnetic fields in laboratory environments. The main advantage of piezoelectric actuation is its wide frequency bandwidth; however, it requires very high excitation voltages (~ 300 V) and, therefore, complex excitation electronics. Wide actuation bandwidths are required for creating insect-scale flapping-wing flyers, but the observed undulation frequencies in anguilliform swimmers do not overpass 10 Hz [22]. Ionic-polymer actuation provides unique new capabilities for soft robotic systems; however, its relatively low force outputs significantly limit its applicability to the development of aquatic propulsion systems. In contrast with other actuators for microrobotics, the actuator that drives the VLEIBot is not only light (6 mg) and fast (up to 30 Hz), but also can generate large forces (~ 84 mN) using very low voltages (5 to 25 V) and simple excitation electronics. To heuristically optimize the hydrodynamic design and operation parameters of the VLEIBot, we used a Vicon motion-capture system to investigate the relationship between the robot’s average speed and tail geometry through a series of characterization experiments. We discovered that, among the cases tested, the fastest speed of $15.1 \text{ mm} \cdot \text{s}^{-1}$ ($0.33 \text{ BI} \cdot \text{s}^{-1}$) is attained using a parabolic tail with a constant aspect ratio of 0.41 and length of 26 mm, undulating at a frequency of 5 Hz.

Simple swimming experiments showed that, due to asymmetrical force production of the SMA-based exciting actuator and high sensitivity to external disturbances, the VLEIBot exhibits low maneuverability. To address this performance challenge, we developed the 90-mg VLEIBot⁺, a modular design that achieves full 2D controllability by using two 6-mg SMA actuators that independently drive two anguilliform-inspired propulsors. From a control perspective, this approach follows the methodology first introduced in [2]. In the case presented here, we achieved high turning capabilities. Using a Vicon motion-capture system, to evaluate and demonstrate the locomotion performance that the VLEIBot⁺ can achieve, we performed several swimming open-loop and closed-loop control experiments. In addition to swimming at speeds on the order of $16 \text{ mm} \cdot \text{s}^{-1}$ ($0.35 \text{ BI} \cdot \text{s}^{-1}$), the VLEIBot⁺ can turn at rates as high as $0.28 \text{ rad} \cdot \text{s}^{-1}$. The measured *root-mean-square* (RMS) tracking-error values are as low as 3.94 mm when operating at the optimal frequency of 5 Hz. These results are highly significant because it is well known that as the Re decreases, swimming becomes increasingly challenging by the traditional methods used at the human scale ($Re \approx 10^4$) [59]. The VLEIBot and VLEIBot⁺ highlight the possibility of creating mm-to-cm-scale autonomous swimming microrobots that can work together in schools (teams) to perform complex tasks useful to humans.

The rest of the paper is organized as follows. Section II presents the design and fabrication of the 45-mg VLEIBot. Section III describes the experimental setup used in the swimming experiments, and discusses the characterization and performance evaluation of two sets of bioinspired soft propulsors. Section IV discusses the development of the

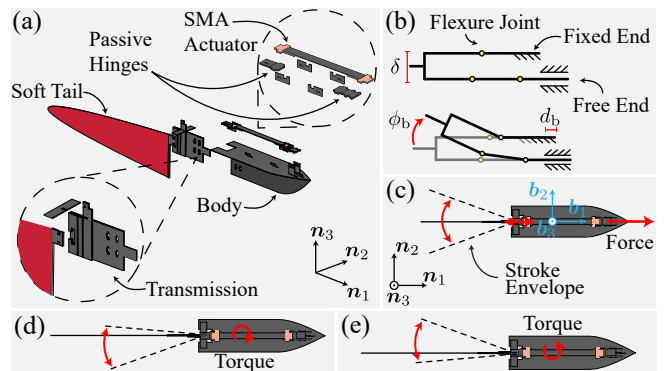


Fig. 2. **Robotic design and functionality.** (a) Components and assembly of the VLEIBot. The VLEIBot is composed of four main components: (i) a rigid body that supports the weight of the robot on water due to surface tension; (ii) a 6-mg HWD SMA-based actuator with passive hinges installed at its two distal ends; (iii) a planar four-bar transmission mechanism that maps the output displacement generated by the SMA-based actuator into the angular oscillation that excites the undulating tail of the swimmer; and, (iv) an anguilliform-inspired soft tail made of fluoropolymer film. The triplet $\{n_1, n_2, n_3\}$ denotes the inertial frame used to describe the kinematics of the system. (b) Transmission functionality. The planar four-bar mechanism can be adjusted to have a constant bias angle, ϕ_b , by shifting the installation point of the fixed end by a distance d_b . (c) Forward locomotion. The VLEIBot is designed to function with a symmetric stroke envelope (sweeping area). The SMA-based actuator produces the periodic displacement output that is mapped by the transmission into the large stroke angles required to undulate the robot’s tail. The triplet $\{b_1, b_2, b_3\}$ denotes the body-fixed frame used to describe the kinematics of the system. (d) Right turn. Theoretically, a right-biased undulation produces a negative torque with respect to the body frame and, as a consequence, a right turn. (e) Left turn. Theoretically, a left-biased undulation produces a positive torque with respect to the body frame and, as a consequence, a left turn.

VLEIBot⁺ and presents closed-loop swimming experiments. Finally, Section V states some conclusions regarding the presented research.

II. DESIGN AND FABRICATION

As shown in Fig. 2(a), the VLEIBot has four main components: (i) a rigid body that supports the weight of the entire robot on water due to surface tension; (ii) a 6-mg SMA-based actuator, which is installed in the robot with passive hinges attached to its two distal ends; (iii) a planar four-bar transmission; and, (iv) a soft tail heuristically designed to generate anguilliform-inspired locomotion. All composing parts were designed and fabricated using the methods described in [6]–[9] and references therein. The body of the robot is made of *carbon fiber* (CF); the actuator is made of CF, FR4, and SMA wires, according to the configuration in [1], [2]; the transmission and hinges are made of CF and Kapton; and, the soft tail is made of 25- μm -thick fluoropolymer film (AirTech A4000R14417). The basic configuration of the body is simply the perpendicular intersection of two flat CF pieces with significant areas relative to their volumes. One piece interacts horizontally with the water and, because of a relatively high surface tension, maintains the robot afloat; the other piece functions as a keel, thus providing stability and high lateral drag compared to that acting on the tail. The 6-mg HWD SMA-based actuator excites the four-bar transmission; the transmission excites the flexible tail, which periodically undulates during swimming to produce thrust. To select the geometrical parameters that maximize the transmission ratio, we used the nonlinear relationship discussed in [60]. Also, we incorporate interchangeability and enforce

alignment in the tail installation process by using a keyway system integrated into the transmission.

As discussed in [1], actuators of the type employed to drive the VLEIBot accumulate a steady-state bias during operation at *pulse-width modulation* (PWM) frequencies higher than 1 Hz because of the limited time available for the composing SMA wires to cool down within an actuation cycle. To address this issue, the transmission is tuned and installed with a fixed bias angle, ϕ_b , as depicted in Fig. 2(b). This bias angle is created by simply displacing the fixed end of the transmission, as graphically defined in Fig. 2(b), by a distance d_b ; namely, $\phi_b = T \cdot d_b$, where T is the transmission ratio. For small displacements, the transmission ratio can be estimated as $T = \delta^{-1}$ [60], where δ is the offset between the fixed and free ends of the mechanism, as graphically defined in Fig. 2(b). In the case of PWM-based Joule heating, because of the ϕ_b adjustment, when the actuator contracts during an actuation cycle, the direction of bending is opposite to that of ϕ_b . This effect allows us to generate a symmetric stroke envelope (sweeping area) with respect to the body-fixed b_1 - b_3 plane, for any given operational frequency, as depicted in Fig. 2(c). Unfortunately, different operational frequencies require different ϕ_b adjustments. Nonetheless, test results indicate that the VLEIBot can achieve straight forward locomotion in open loop after its transmission is tuned for a predefined operational condition. The tuning procedure is very simple. First, we install the transmission with a bias angle of approximately 0.3 rad; then, we excite the VLEIBot with a signal that produces significant forward locomotion, selected through the tests presented and discussed in Section III; last, we visually determine the magnitude and direction of ϕ_b required to adjust the transmission. We repeat this process, if necessary, until we observe a symmetric stroke envelope.

By generating a symmetric stroke envelope, we ensure that the total hydrodynamic force produced by the undulating tail has a lateral average of zero in steady state and, therefore, its resulting average direction is ideally aligned with the body-fixed b_1 axis. However, due to external disturbances, such as the pull of the tether wire and wind gusts, the VLEIBot often deviates from a given straight path in open loop operation. This observation highlights the need for feedback control, even after the stroke envelope has been tuned. Theoretically, basic control strategies can be implemented by simply modulating the PWM actuator-exciting signal and thus create an asymmetrical tail undulation with respect to the body-fixed b_1 axis (see Fig. 2(c)). As illustrated in Figs. 2(d) and (e), theoretically, an asymmetrical stroke envelope produces a torque that rotates the robot during swimming, thus endowing it with turning capabilities and controllability in 2D. Unfortunately, empirical evidence indicates that this turning ability of the robot is highly sensitive to slight miscalibration of the stroke envelope and external disturbances. Fortunately, as discussed in Section IV, this steerability issue can be solved with a modular design that puts together two VLEIBot platforms to create the VLEIBot⁺.

III. TAIL CHARACTERIZATION

A. Experimental Setup and Swimming Tests

An illustration of the experimental setup used in the swimming tests is shown in Fig. 3(a). As seen here, to

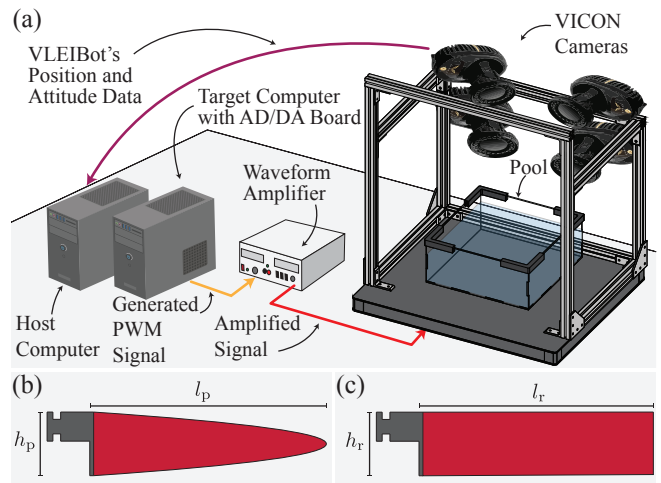


Fig. 3. **Experimental setup used in the tail-characterization swimming tests.** (a) Experimental setup. A Simulink Real-Time host-target system and an AD/DA board (National Instruments PCI-6229) are used to generate the PWM signal that excites the robot. This signal is then filtered through a waveform amplifier (Accel Instruments TS250-02) to provide the power necessary to periodically Joule heat the SMA-based actuator that drives the VLEIBot. During the swimming tests, the VLEIBot is placed in a pool filled with water and a four-VK16-camera Vicon motion-capture system is used to measure the instantaneous position and orientation of the robot at a rate of 250 Hz. (b) Parameters of the parabolic tails with constant aspect ratio. For the tail-characterization experiments, we kept the aspect ratio constant at $R_p = 0.41$ and varied the tail length, l_p , in increments of 2 mm over the range [0 : 28] mm. The height h_p directly depends on the length l_p . (c) Parameters of the rectangular tails with constant height. For the tail-characterization experiments, we kept the height, h_r , constant at 4 mm and varied the length, l_r , in increments of 5 mm over the range [0 : 50] mm.

generate the PWM signal that excites the robot, and for signal processing and control, we use a Simulink Real-Time host-target system and a National Instruments PCI-6229 *analog-digital/digital-analog* (AD/DA) board. After the PWM signal is generated, this is filtered through a waveform amplifier (Accel Instruments TS250-02) to supply the power necessary to cyclically Joule heat the SMA material of the robot's actuator. During the experiments, a VLEIBot prototype is placed in a pool filled with water while a four-VK16-camera Vicon motion-capture system measures and records its instantaneous position, \mathbf{r} , and attitude at a frequency of 250 Hz. We estimate the velocity, \mathbf{v} , and angular velocity, $\boldsymbol{\omega}$, of the robot using a discrete-time derivative algorithm and, then, these data are further processed using a low-pass *finite impulse response* (FIR) filter with order 10^3 and cutoff frequency of 40 Hz. For consistency with the Vicon system, the host-target system samples, processes, generates, and records signals at 250 Hz.

To characterize the effects of tail geometry and size on the swimming performance of the VLEIBot, we experimentally investigated two basic tail geometries: (i) a low-aspect-ratio parabolic-shaped tail, loosely inspired by the tails of the European eel and young ACF tadpole; and, (ii) a thin rectangular-shaped tail, loosely inspired by the tail of the yellow-bellied sea snake. During the characterization process, we tested several aspect ratios of the two basic geometries selected, over a range of excitation frequencies. Then, using the measured data, we heuristically determined the best-performing tail for the VLEIBot regarding speed of locomotion. In the tail-characterization experiments and

analyses, we estimate the Reynolds number as

$$Re = \frac{lv\rho}{\mu}, \quad (1)$$

in which l and v are the length (including the tail) and speed of the swimmer, respectively; and, ρ and μ are the density and dynamic viscosity of water at 20 °C, respectively. Considering all achieved speeds and tested tails, the Re is inside the range $[10^{-1} : 10^3]$. As a reference, the Re for the swimming of the young ACF tadpole is on the order of 250 [21]. Also, similarly to the VLEIBot, the young ACF tadpole has a wide rigid head and a thin highly-flexible tail. Furthermore, the lack of osseous or cartilaginous support in their tails [23], prompt us to speculate that the young ACF tadpoles might take advantage of FSI phenomena to locomote.

The similarities between the VLEIBot and young ACF tadpoles are the main reasons to use the anatomy of these animals as a model for tail design. Specifically, we selected a constant aspect ratio, specified as $\mathcal{R}_p = h_p^2 \cdot A_p^{-1}$, where h_p and A_p are respectively the height and area of the tail, both graphically defined in Fig. 3(b). Assuming a parabolic shape, we determined that the aspect ratio is approximately 0.41 for the tails of young ACF tadpoles. By keeping the aspect ratio of each tested tail fixed, its height becomes a function of its length, l_p , which is defined in Fig. 3(b). With this in mind, for the constant aspect ratio $\mathcal{R}_p = 0.41$, we made and tested 14 different tails in the set $[2 : 2 : 28]$ mm. To design the tested rectangular tails, loosely inspired by the tail geometry of yellow-bellied sea snakes, we simply selected the constant height $h_r = 4$ mm, as defined in Fig. 3(c), and varied the length, l_r , as illustrated in Fig. 3(c), over the range $[5 : 50]$ mm in increments of 5 mm. To evaluate the performance associated with the tested tails, we measured the average forward speed of the robot across all the considered tail lengths and shapes. For each tested pair of exciting frequency and tail shape, we performed 10 swimming tests. The tested frequencies are 1, 5, 10, 15, and 20 Hz with a heuristically chosen duty cycle—defined as the percentage of the PWM period for which the signal is at its *on* voltage—of 8%, for the excitation of 1 Hz, and of 10%, for the other tested frequencies. An *on* voltage of 22 V was selected such that the actuator is provided with 250 mA of current; higher current values were observed to burn the thin 53 AWG tether wires that power the robot. For analysis, the average speed of each swimming experiment was computed from 20 s of data. Then, we found the mean and *empirical standard deviation* (ESD) of the 10 tests corresponding to each pair of PWM frequency and tail shape. These data are summarized in Fig. 4 and discussed next.

B. Results and Discussion

The experimental data corresponding to the parabolic tails with a constant aspect ratio $\mathcal{R}_p = 0.41$ are shown in Fig. 4(a). Here, we can clearly see a trend; over the range $[2 : 26]$ mm, as the tail length, l_p , increases, the average speed, \bar{v} , tends to increase. After passing a length of 26 mm, \bar{v} tends to decrease because of the relatively high weight of the tail compared to that of the robot. With a frequency of 5 Hz and $l_p = 26$ mm, we obtained the best swimming performance in terms of speed, $15.1 \text{ mm} \cdot \text{s}^{-1}$ ($0.33 \text{ Bl} \cdot \text{s}^{-1}$). The experimental data corresponding to the rectangular tails

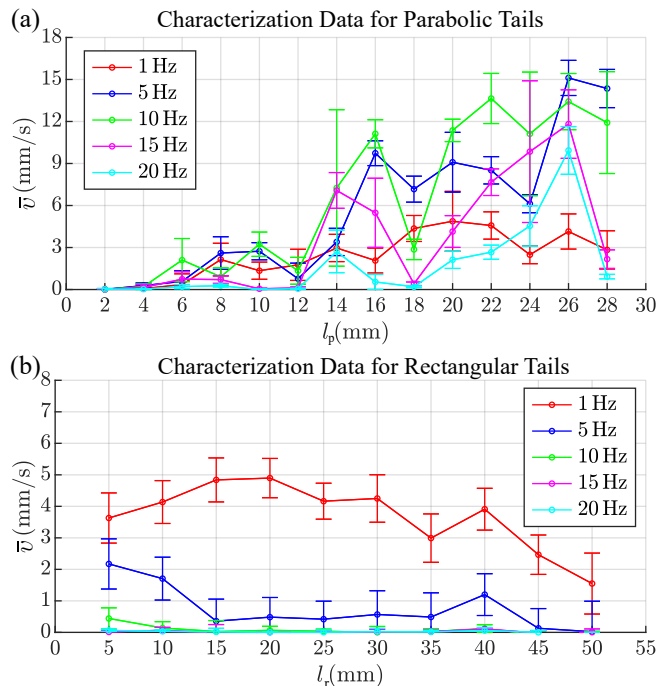


Fig. 4. **Tail-characterization data.** (a) Characterization of parabolic tails with constant aspect ratio. During the swimming tests, the aspect ratio was kept constant at $\mathcal{R}_p = 0.41$, while we investigated the relationship between tail length and average forward speed across frequencies of 1, 5, 10, 15, and 20 Hz. We see an increasing trend in average speed as tail length increases. At the tail length of 26 mm and frequency of 5 Hz, we measured the maximum average speed of $15.1 \text{ mm} \cdot \text{s}^{-1}$ ($0.33 \text{ Bl} \cdot \text{s}^{-1}$). When the tail length, l_p , was increased further, the weight of the tail tended to drag the robot under the surface of the water. (b) Characterization of rectangular tails with constant height. During the swimming tests, the tail height was kept constant at $h_r = 4$ mm, while we investigated the relationship between tail length and speed. We varied the tail length in increments of 5 mm over the range $[5 : 50]$ mm. It can be observed that high-frequency actuation is not able to produce thrust with any of the investigated tails, and 1 Hz is the best actuation frequency for all the tested profiles. At the length of 20 mm, we see the best swimming performance of $4.7 \text{ mm} \cdot \text{s}^{-1}$ ($0.12 \text{ Bl} \cdot \text{s}^{-1}$).

with constant height $h_r = 4$ mm are shown in Fig. 4(b). In these tests, for all tail lengths, the best frequency is 1 Hz; for this frequency, the best average speed is $4.7 \text{ mm} \cdot \text{s}^{-1}$ ($0.12 \text{ Bl} \cdot \text{s}^{-1}$), corresponding to a tail length of 20 mm. At frequencies higher than 5 Hz, essentially, no locomotion can be produced with the tested rectangular tails. Overall, the swimming performances achieved with the parabolic tails are significantly better than those obtained with the rectangular tails. Through this heuristic process, we selected the parabolic 26-mm tail for the VLEIBot prototype. Photographic composites of frames taken at intervals of 6 s over 24 s, with the *optimized* VLEIBot swimming at 1 and 5 Hz are shown in Figs. 5(a) and (b), respectively. Video footage of these two experiments are shown in the accompanying supplementary movie.

IV. THE VLEIBOT⁺: A CONTROL APPROACH

A. Controllable Design

As explained in previous sections, after multiple open-loop swimming experiments, we determined that the VLEIBot design lacks the steerability required to execute high-speed turning maneuvers. To address this issue, we developed the 90-mg dual-propulsor VLEIBot⁺, which is fast, highly

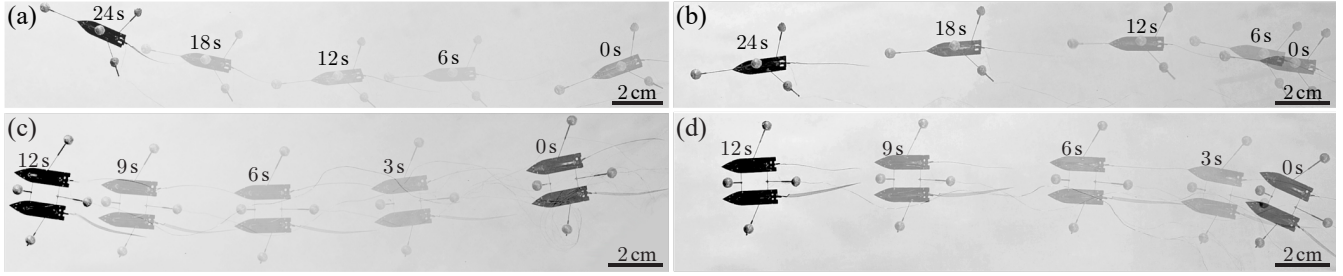


Fig. 5. **Locomotion experiments performed using optimized parabolic 26-mm tail with constant aspect ratio of 0.41.** (a) Photographic composite from video footage showing the VLEIBot swimming at 1 Hz. The duty cycle of the driving PWM signal is 8%. (b) Photographic composite from video footage showing the VLEIBot swimming at 5 Hz. The duty cycle of the driving PWM signal is 12%. (c) Photographic composite from video footage showing the VLEIBot⁺ swimming at 1 Hz. The duty cycles of the driving PWM signals are 8%. (d) Photographic composite from video footage showing the VLEIBot⁺ swimming at 5 Hz. The duty cycles of the driving PWM signals are 12%. Video footage of these experiments can be viewed in the accompanying supplementary movie.

maneuverable, and fully controllable in the 2D space. Photographic composites of frames taken at intervals of 3 s over 12 s, with a VLEIBot⁺ prototype swimming at 1 and 5 Hz, are shown in Figs. 5(c) and (d), respectively. Video footage of these two experiments are shown in the accompanying supplementary movie. A VLEIBot⁺ is built by connecting two VLEIBot prototypes in the parallel and symmetrical configuration depicted in Fig. 6(a), using two CF beams. The separation between the two composing bodies is chosen to be 6 mm in order to enable the cancelation, due to symmetry, of undesired torques produced by the undulating tails during forward locomotion; this notion is illustrated in Fig. 6(b). The swimming tests corresponding to Figs. 5(c) and (d) compellingly demonstrate an *almost* perfect cancelation of the opposing torques generated by the two sides of the tested prototype. Due to this effect, VLEIBot⁺ prototypes are fully controllable in the 2D space.

B. Control Strategy

To enable the VLEIBot⁺ to execute turning maneuvers and track references in the 2D space, we implemented the control scheme in Fig. 6(c), which is almost identical to that in [2]. Here, the pair $\{r_1, r_2\}$ (first two components of \mathbf{r}) is the instantaneous position of the robot's body-fixed frame in the 2D space relative to the inertial frame, and ψ is the instantaneous yaw angle, measured with the Vicon system. In this scheme, the lateral position controller computes the desired heading according to

$$\psi_d = k_{p,2} r_{e,2} + k_{i,2} \int_0^t r_{e,2} d\tau, \quad (2)$$

where $k_{p,2}$ and $k_{i,2}$ are proportional and integral controller gains; and, $r_{e,2} = r_{d,2} - r_2$ is the lateral-position error computed as the difference between the desired and measured lateral positions, $r_{d,2}$ and r_2 , respectively. The heading controller computes the control signal $u_\psi = k_{p,\psi} \psi_e$, where $k_{p,\psi}$ is a proportional controller gain and $\psi_e = \psi_d - \psi$ is the yaw-angle error computed as the difference between the desired and current yaw angles, ψ_d and ψ , respectively. Last, the actuator mapping receives u_ψ and a constant u_v , and maps them into the duty-cycle values u_l and u_r used to define the PWM signals that respectively drive the left and right actuators of the robot, according to

$$\begin{bmatrix} u_l \\ u_r \end{bmatrix} = \begin{bmatrix} k_l & -k_l \\ k_r & k_r \end{bmatrix} \begin{bmatrix} u_v \\ u_\psi \end{bmatrix}, \quad (3)$$

where k_l and k_r are tunable mapping constants.

C. Swimming Experiments

To evaluate and demonstrate the swimming capabilities of the VLEIBot⁺, we used the same setup depicted in Fig. 3(a) and described in Section III-A. Fig. 7(a) summarizes the experimental data of a VLEIBot⁺ prototype swimming for 20 s at 5 Hz in open loop, after being tuned to nominally follow a straight path. In this test, the two robot's actuators were excited using PWM signals with an *on* voltage of 22 V and duty cycle of 12%. Fig. 7(a.i) shows a photographic composite of frames taken at intervals of 5 s, of the swimming test. And, Figs. 7(a.ii) and (a.iii) show the robot's 2D position and lateral-position error during the test. The maximum average forward speed, computed over a 1 second window, is $13.6 \text{ mm} \cdot \text{s}^{-1}$ ($0.30 \text{ Bl} \cdot \text{s}^{-1}$). For this experiment, the RMS value of the lateral-position error is 20.4 mm. Fig. 7(b) summarizes the experimental data of a VLEIBot⁺ prototype swimming for 20 s at 5 Hz in closed loop, following a straight-line reference and driven by the controller described in Section IV-B. In this case, $k_{p,2} = 2 \text{ rad} \cdot \text{m}^{-1}$, $k_{i,2} = 0.1 \text{ rad} \cdot \text{m}^{-1}$, $k_\psi = 0.2 \text{ rad}^{-1}$, $u_v = 0.11$ (per unit), $k_l = 1$, and $k_r = 1$; the *on* PWM voltage was set at 22 V. Fig. 7(b.i) shows a photographic composite of frames taken at intervals of 5 s, of the swimming test. And, Figs. 7(b.ii) and (b.iii) show the robot's position in the 2D space and lateral-position error during the test. The maximum average forward speed is $14.8 \text{ mm} \cdot \text{s}^{-1}$ ($0.32 \text{ Bl} \cdot \text{s}^{-1}$), and the corresponding RMS value of the lateral-position error is 3.94 mm; this RMS-error value represents a decrease of 80% with respect to that obtained in open loop.

Fig. 7(c) summarizes the experimental data of a VLEIBot⁺ prototype during the execution of a 90-degree left-turn maneuver. Fig. 7(c.i) shows a photographic composite of frames taken at intervals of 6 s, of the swimming test. And, Figs. 7(c.ii) and (c.iii) show the robot's position in the 2D space and lateral-position error during the test. The measured maximum average speed and turning rate are $16.1 \text{ mm} \cdot \text{s}^{-1}$ ($0.35 \text{ Bl} \cdot \text{s}^{-1}$) and $0.25 \text{ rad} \cdot \text{s}^{-1}$ respectively, and the corresponding RMS value of the lateral-position error is 20.8 mm. Fig. 7(d) summarizes the experimental data of a VLEIBot⁺ prototype during the execution of a 90-degree right-turn maneuver. Fig. 7(d.i) shows a photographic composite of frames taken at intervals of 6 s, of the swimming test. And, Figs. 7(d.ii) and (d.iii) show the robot's position in the 2D space and lateral-position error during the test.

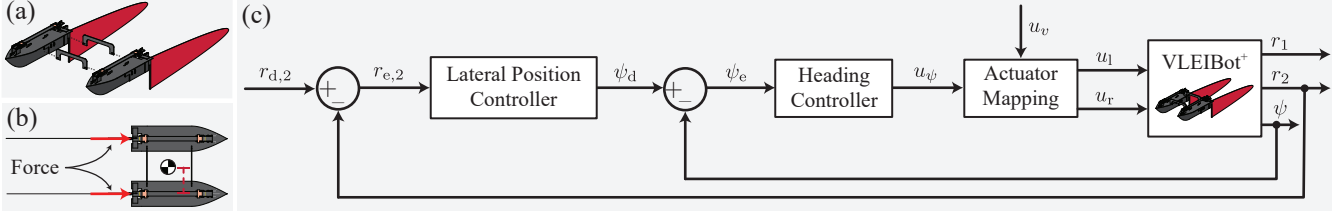


Fig. 6. **The VLEIBot⁺ and block diagram of the control scheme.** (a) Assembly of two VLEIBots in parallel to create the VLEIBot⁺. (b) Turning functionality of the VLEIBot⁺. The separation between the two propulsors of the VLEIBot⁺ enables a dependable production of turning torque by introducing a net force differential. (c) Architecture used to control the VLEIBot⁺ during swimming. The lateral position controller receives as input the lateral position error, $r_{e,2} = r_{d,2} - r_2$, and computes the desired yaw angle, ψ_d . Next, the heading controller receives as input the yaw-angle error, $\psi_e = \psi_d - \psi$, and computes the heading control signal, u_ψ . Last, the actuator mapping receives as inputs u_ψ and the constant u_v , and maps them into the duty cycles u_l and u_r , which are used to define the PWM signals that excite the left and right SMA-based actuators of the robot, respectively.

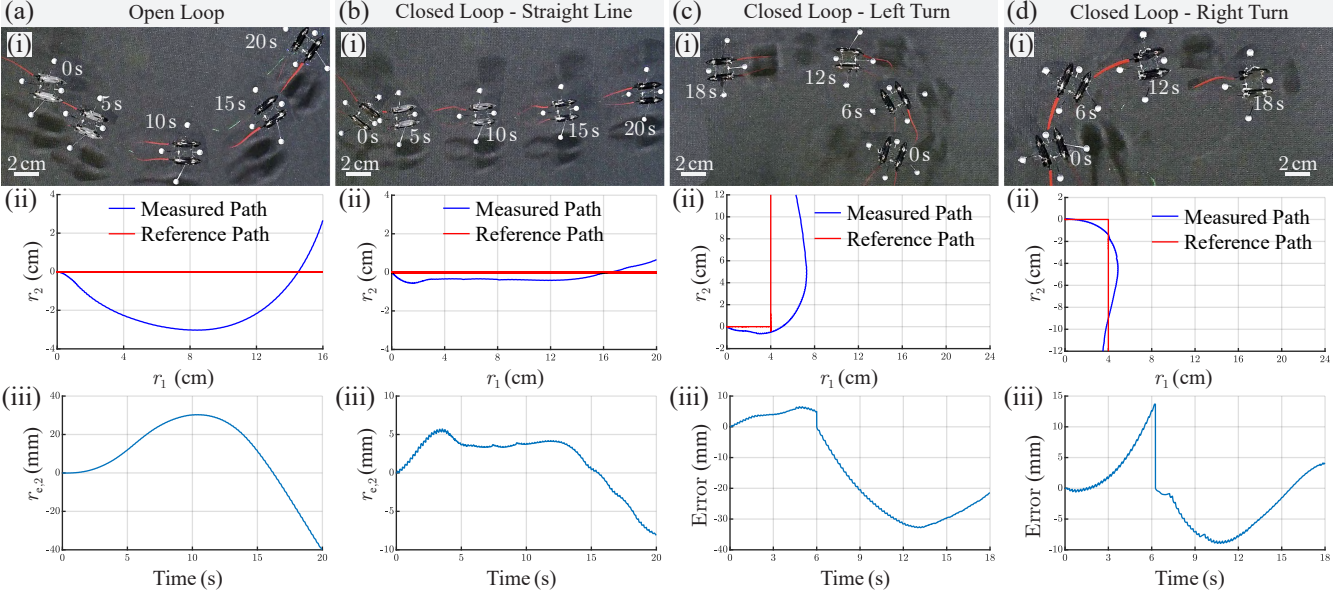


Fig. 7. **VLEIBot⁺ locomotion experiments.** (a) 20-s open-loop swimming experiment at 5 Hz. (i) Photographic composite of frames taken at intervals of 5 s from video footage of the VLEIBot⁺ swimming forward in open loop. Both actuators of the robot were excited using a 5-Hz PWM signal with a duty cycle of 12%. (ii) Measured position of the VLEIBot⁺ over the course of the open-loop experiment. (iii) Lateral error of the VLEIBot⁺ over the course of the experiment. We measured an RMS-error value of 20.4 mm. (b) 20-s closed-loop swimming experiment at 5 Hz. (i) Photographic composite of frames taken at intervals of 5 s from video footage of the VLEIBot⁺ swimming forward in closed loop. (ii) Measured position of the VLEIBot⁺ over the course of the closed-loop experiment. We measured a maximum angular turning rate of $0.25 \text{ rad} \cdot \text{s}^{-1}$. (iii) Lateral error of the VLEIBot⁺ over the course of the experiment. We measured an RMS-error value of 20.8 mm. (c) 18-s closed-loop left-turn experiment at 5 Hz. (i) Photographic composite of frames taken at intervals of 6 s from video footage of the VLEIBot⁺ swimming in closed loop. (ii) Measured position of the VLEIBot⁺ over the course of the closed-loop experiment. We measured a maximum angular turning rate of $0.25 \text{ rad} \cdot \text{s}^{-1}$. (iii) Lateral error of the VLEIBot⁺ over the course of the experiment. We measured an RMS-error value of 20.8 mm. (d) 18-s closed-loop right-turn experiment at 5 Hz. (i) Photographic composite of frames taken at intervals of 6 s from video footage of the VLEIBot⁺ swimming in closed loop. (ii) Measured position of the VLEIBot⁺ over the course of the closed-loop experiment we measure a maximum angular turning rate of $0.28 \text{ rad} \cdot \text{s}^{-1}$. (iii) Lateral error of the VLEIBot⁺ over the course of the experiment. We measured an RMS-error value of 5.45 mm. Video footage of the experiments can be viewed in the accompanying supplementary movie.

The measured maximum average speed and turning rate are $10.0 \text{ mm} \cdot \text{s}^{-1}$ ($0.22 \text{ Bl} \cdot \text{s}^{-1}$) and $0.28 \text{ rad} \cdot \text{s}^{-1}$, respectively, and the corresponding RMS value of the lateral-position error is 5.45 mm.

V. CONCLUSIONS

We presented the design and development of two new microbotic swimmers: the 45-mg/23-mm³ VLEIBot and its high-performance evolution, the 90-mg/47-mm³ VLEIBot⁺. We designed the propulsor for the VLEIBot drawing inspiration from the anguilliform swimming mode exhibited by some aquatic animals such as the European eel, yellow-bellied sea snake, and young ACF tadpole. The final heuristically-optimized propulsor design, loosely inspired by the tail of the young ACF tadpole, has a parabolic shape, a length of 26 mm, and an aspect ratio of 0.41, and produces

the best results in terms of speed at an actuation frequency of 5 Hz. We arrived to these parameters after performing hundreds of tail-characterization experiments. With the optimized propulsor, the VLEIBot can achieve forward speeds as high as $15.1 \text{ mm} \cdot \text{s}^{-1}$ ($0.33 \text{ Bl} \cdot \text{s}^{-1}$) at a frequency of 5 Hz; however, its maneuverability is extremely limited. With optimized propulsors, the VLEIBot⁺ can achieve forward speeds as high as $16.1 \text{ mm} \cdot \text{s}^{-1}$ ($0.35 \text{ Bl} \cdot \text{s}^{-1}$) at a frequency of 5 Hz; furthermore, because of its high maneuverability in the 2D space, it can perform maneuvers at angular speeds as high as $0.28 \text{ rad} \cdot \text{s}^{-1}$. To our best knowledge, the VLEIBot and VLEIBot⁺ are the first self-propelled anguilliform-inspired microswimmers. Furthermore, these robots are two of the very few that fully exploit FSI phenomena to generate the waves that propagate along their tails to produce locomotion.

REFERENCES

- [1] X.-T. Nguyen, A. A. Calderón, A. Rigo, J. Z. Ge, and N. O. Pérez-Arancibia, "SMALLBug: A 30-mg Crawling Robot Driven by a High-Frequency Flexible SMA Microactuator," *IEEE Robot. Automat. Lett.*, vol. 5, no. 4, pp. 6796–6803, Oct. 2020.
- [2] R. M. Bena, X.-T. Nguyen, A. A. Calderón, A. Rigo, and N. O. Pérez-Arancibia, "SMARTI: A 60-mg Steerable Robot Driven by High-Frequency Shape-Memory Alloy Actuation," *IEEE Robot. Automat. Lett.*, vol. 6, no. 4, pp. 8173–8180, Oct. 2021.
- [3] C. K. Trygstad, X.-T. Nguyen, and N. O. Pérez-Arancibia, "A New 1-mg Fast Unimorph SMA-Based Actuator for Microrobotics," in *Proc. IEEE/RSJ Int. Conf. Intell. Robots Syst. (IROS)*, Detroit, MI, USA, Oct. 2023, pp. 2693–2700.
- [4] N. O. Pérez-Arancibia, K. Y. Ma, K. C. Galloway, J. D. Greenberg, and R. J. Wood, "First controlled vertical flight of a biologically inspired microrobot," *Bioinspir. Biomim.*, vol. 6, no. 3, Sep. 2011, Art. no. 036009.
- [5] N. O. Pérez-Arancibia, P.-E. J. Duhamel, K. Y. Ma, and R. J. Wood, "Model-Free Control of a Hovering Flapping-Wing Microrobot," *J. Intell. Robot. Syst.*, vol. 77, no. 1, pp. 95–111, Jan. 2015.
- [6] X. Yang, Y. Chen, L. Chang, A. A. Calderón, and N. O. Pérez-Arancibia, "Bee⁺: A 95-mg Four-Winged Insect-Scale Flying Robot Driven by Twinned Unimorph Actuators," *IEEE Robot. Automat. Lett.*, vol. 4, no. 4, pp. 4270–4277, Oct. 2019.
- [7] R. M. Bena, X.-T. Nguyen, X. Yang, A. A. Calderón, Y. Chen, and N. O. Pérez-Arancibia, "A Multiplatform Position Control Scheme for Flying Robotic Insects," *J. Intell. Robot. Syst.*, vol. 105, no. 1, May 2022, Art. no. 19.
- [8] R. M. Bena, X. Yang, A. A. Calderón, and N. O. Pérez-Arancibia, "High-Performance Six-DOF Flight Control of the Bee⁺: An Inclined-Stroke-Plane Approach," *IEEE Trans. Robot.*, vol. 39, no. 2, pp. 1668–1684, Apr. 2023.
- [9] X. Yang, L. Chang, and N. O. Pérez-Arancibia, "An 88-milligram insect-scale autonomous crawling robot driven by a catalytic artificial muscle," *Sci. Robot.*, vol. 5, no. 45, Aug. 2020, Art. no. eaba0015.
- [10] S. B. Fuller, Z. E. Teoh, P. Chirattananon, N. O. Pérez-Arancibia, J. Greenberg, and R. J. Wood, "Stabilizing air dampers for hovering aerial robotics: design, insect-scale flight tests, and scaling," *Auton. Robot.*, vol. 41, no. 8, pp. 1555–1573, Dec. 2017.
- [11] N. O. Pérez-Arancibia, P.-E. J. Duhamel, K. Y. Ma, and R. J. Wood, "Model-Free Control of a Hovering Flapping-Wing Microrobot," *J. Intell. Robot. Syst.*, vol. 77, no. 1, pp. 95–111, Jan. 2015.
- [12] —, "Model-Free Control of a Flapping-Wing Flying Microrobot," in *Proc. 16th Int. Conf. Adv. Robot. (ICAR)*, Montevideo, Uruguay, Nov. 2013, pp. 1–8.
- [13] P.-E. J. Duhamel, N. O. Pérez-Arancibia, G. L. Barrows, and R. J. Wood, "Biologically Inspired Optical-Flow Sensing for Altitude Control of Flapping-Wing Microrobots," *IEEE/ASME Trans. Mechatron.*, vol. 18, no. 2, pp. 556–568, Apr. 2013.
- [14] Z. E. Teoh, S. B. Fuller, P. Chirattananon, N. O. Pérez-Arancibia, J. D. Greenberg, and R. J. Wood, "A Hovering Flapping-Wing Microrobot with Altitude Control and Passive Upright Stability," in *Proc. IEEE/RSJ Int. Conf. Intell. Robots Syst. (IROS)*, Vilamoura, Algarve, Portugal, Oct. 2012, pp. 3209–3216.
- [15] P.-E. J. Duhamel, N. O. Pérez-Arancibia, G. L. Barrows, and R. J. Wood, "Altitude Feedback Control of a Flapping-Wing Microrobot Using an On-Board Biologically Inspired Optical Flow Sensor," in *Proc. IEEE Int. Conf. Robot. Autom. (ICRA)*, Saint Paul, Minnesota, USA, May 2012, pp. 4228–4235.
- [16] N. O. Pérez-Arancibia, J. P. Whitney, and R. J. Wood, "Lift Force Control of a Flapping-Wing Microrobot," in *Proc. Amer. Control Conf. (ACC)*, San Francisco, CA, USA, Jun. 2011, pp. 4761–4768.
- [17] N. O. Pérez-Arancibia, P. Chirattananon, B. M. Finio, and R. J. Wood, "Pitch-Angle Feedback Control of a Biologically Inspired Flapping-Wing Microrobot," in *Proc. Int. Conf. Robot. Biomim. (RO-BIO)*, Karon Beach, Thailand, Dec. 2011, pp. 1495–1502.
- [18] N. O. Pérez-Arancibia, J. P. Whitney, and R. J. Wood, "Lift Force Control of Flapping-Wing Microrobots Using Adaptive Feedforward Schemes," *IEEE/ASME Trans. Mechatron.*, vol. 18, no. 1, pp. 155–168, Feb. 2013.
- [19] A. P. Palstra and G. E. E. J. M. van den Thillart, "Swimming physiology of European silver eels (*Anguilla anguilla* L.): energetic costs and effects on sexual maturation and reproduction," *Fish Physiol. Biochem.*, vol. 36, no. 3, pp. 297–322, Apr. 2010.
- [20] J. B. Graham, W. R. Lowell, I. Rubinfoff, and J. Motta, "Surface and Subsurface Swimming of the Sea Snake *Pelamis platurus*," *J. Exp. Biol.*, vol. 127, no. 1, pp. 27–44, Jan. 1986.
- [21] A. Roberts, N. A. Hill, and R. Hicks, "Simple Mechanisms Organise Orientation of Escape Swimming in Embryos and Hatchling Tadpoles of *Xenopus laevis*," *J. Exp. Biol.*, vol. 203, no. 12, pp. 1869–1885, Jun. 2000.
- [22] N. B. Tack, K. T. Du Clos, and B. J. Gemmill, "Anguilliform Locomotion across a Natural Range of Swimming Speeds," *Fluids*, vol. 6, no. 3, Mar. 2021, Art. no. 127.
- [23] H. Liu, R. Wassersug, and K. Kawachi, "The Three-Dimensional Hydrodynamics of Tadpole Locomotion," *J. Exp. Biol.*, vol. 200, no. 22, pp. 2807–2819, Nov. 1997.
- [24] T. Fukuda, H. Hosokai, and I. Kikuchi, "Distributed Type of Actuators by Shape Memory Alloy and its Application to Underwater Mobile Robotic Mechanism," in *Proc. IEEE Int. Conf. Robot. Autom. (ICRA)*, Cincinnati, OH, USA, May 1990, pp. 1316–1321.
- [25] L. J. Garner, L. N. Wilson, D. C. Lagoudas, and O. K. Rediniotis, "Development of a shape memory alloy actuated biomimetic vehicle," *Smart Mater. Struct.*, vol. 9, no. 5, pp. 673–683, Oct. 2000.
- [26] C. Rossi, J. Colorado, W. Coral, and A. Barrientos, "Bending continuous structures with SMAs: a novel robotic fish design," *Bioinspir. Biomim.*, vol. 6, no. 4, Dec. 2011, Art. no. 045005.
- [27] K.-J. Cho, E. Hawkes, C. Quinn, and R. J. Wood, "Design, fabrication and analysis of a body-caudal fin propulsion system for a microrobotic fish," in *Proc. IEEE Int. Conf. Robot. Autom. (ICRA)*, Pasadena, CA, USA, May 2008, pp. 706–711.
- [28] Z. Wang, G. Hang, J. Li, Y. Wang, and K. Xiao, "A micro-robot fish with embedded SMA wire actuated flexible biomimetic fin," *Sens. Actuators A: Phys.*, vol. 144, no. 2, pp. 354–360, Jun. 2008.
- [29] L. Shi, S. Guo, and K. Asaka, "A Novel Jellyfish-like Biomimetic Microrobot," in *Proc. IEEE/ICME Int. Conf. Comp. Med. Eng. (CME)*, Gold Coast, QLD, Australia, Jul. 2010, pp. 277–281.
- [30] D. Byun, J. Choi, K. Cha, J.-O. Park, and S. Park, "Swimming microrobot actuated by two pairs of Helmholtz coils system," *Mechatronics*, vol. 21, no. 1, pp. 357–364, Feb. 2011.
- [31] Q. Ze, S. Wu, J. Dai, S. Leanza, G. Ikeda, P. C. Yang, G. Iaccarino, and R. R. Zhao, "Spinning-enabled wireless amphibious origami millirobot," *Nat. Commun.*, vol. 13, Jun. 2022, Art. no. 3118.
- [32] J. Chen, H. Hu, and Y. Wang, "Magnetic-driven 3D-printed biodegradable swimming microrobots," *Smart Mater. Struct.*, vol. 32, no. 8, Jul. 2023, Art. no. 085014.
- [33] L. Tan and D. J. Cappelleri, "Design, Fabrication, and Characterization of a Helical Adaptive Multi-Material MicroRobot (HAMMR)," *IEEE Robot. Automat. Lett.*, vol. 8, no. 3, pp. 1723–1730, Mar. 2023.
- [34] S. N. Tabatabaei, J. Lapointe, and S. Martel, "Shrinkable Hydrogel-Based Magnetic Microrobots for Interventions in the Vascular Network," *Adv. Robot.*, vol. 25, no. 8, pp. 1049–1067, Apr. 2011.
- [35] S. Fusco, M. S. Sakar, S. Kennedy, C. Peters, R. Bottani, F. Starsich, A. Mao, G. A. Sotiriou, S. Pané, S. E. Pratsinis, D. Mooney, and B. J. Nelson, "An integrated microrobotic platform for on-demand, targeted therapeutic interventions," *Adv. Mater.*, vol. 26, no. 6, pp. 952–957, Feb. 2014.
- [36] H. Li, J. Tan, and M. Zhang, "Dynamics Modeling and Analysis of a Swimming Microrobot for Controlled Drug Delivery," *IEEE Trans. Autom. Sci. Eng.*, vol. 6, no. 2, pp. 220–227, Apr. 2009.
- [37] F. Z. Temel and S. Yesilyurt, "Confined swimming of bio-inspired microrobots in rectangular channels," *Bioinspir. Biomim.*, vol. 10, no. 1, Feb. 2015, Art. no. 016015.
- [38] S. Palagi, V. Pensabene, L. Beccai, B. Mazzolai, A. Menciassi, and P. Dario, "Design and development of a soft magnetically-propelled swimming microrobot," in *Proc. IEEE Int. Conf. Robot. Autom. (ICRA)*, Shanghai, China, May 2011, pp. 5109–5114.
- [39] O. S. Pak, W. Gao, J. Wang, and E. Lauga, "High-speed propulsion of flexible nanowire motors: Theory and experiments," *Soft Matter*, vol. 7, no. 18, Sep. 2011, Art. no. 8169.
- [40] R. Dreyfus, J. Baudry, M. L. Roper, M. Fermigier, H. A. Stone, and J. Bibette, "Microscopic artificial swimmers," *Nature*, vol. 437, no. 6, pp. 862–865, Oct. 2005.
- [41] W. Gao, S. Sattayasamitsathit, K. M. Manesh, D. Weihs, and J. Wang, "Magnetically Powered Flexible Metal Nanowire Motors," *J. Am. Chem. Soc.*, vol. 132, no. 41, pp. 14403–14405, Sep. 2010.
- [42] T. Xu, G. Hwang, N. Andreff, and S. Régnier, "The rotational propulsion characteristics of scaled-up helical microswimmers with different heads and magnetic positioning," in *Proc. IEEE/ASME Int. Conf. Adv. Intell. Mechatron. (AIM)*, Wollongong, NSW, Australia, Jul. 2013, pp. 1114–1120.
- [43] A. Ghosh and P. Fischer, "Controlled Propulsion of Artificial Magnetic Nanostructured Propellers," *Nano Lett.*, vol. 9, no. 6, pp. 2243–2245, May 2009.
- [44] C. E. Sing, L. Schmid, M. F. Schneider, and A. Alexander-Katz, "Controlled surface-induced flows from the motion of self-assembled colloidal walkers," *Proc. Natl. Acad. Sci.*, vol. 107, no. 2, pp. 535–540, Dec. 2009.
- [45] L. Zhang, T. Petit, Y. Lu, B. E. Kratochvil, K. E. Peyer, R. Pei, J. Lou, and B. J. Nelson, "Controlled Propulsion and Cargo Transport of Rotating Nickel Nanowires near a Patterned Solid Surface," *ACS Nano*, vol. 4, no. 10, pp. 6228–6234, Sep. 2010.

- [46] W. Liu, X. Jia, F. Wang, and Z. Jia, "An in-pipe wireless swimming microrobot driven by giant magnetostrictive film," *Sens. Actuators A: Phys.*, vol. 160, no. 2, pp. 101–108, May 2010.
- [47] P. Tierno, R. Golestanian, I. Pagonabarraga, and F. Sagués, "Magnetically Actuated Colloidal Microswimmers," *J. Phys. Chem. B*, vol. 112, no. 51, pp. 16 525–16 528, Nov. 2008.
- [48] S. Floyd, C. Pawashe, and M. Sitti, "An Untethered Magnetically Actuated Micro-Robot Capable of Motion on Arbitrary Surfaces," in *Proc. IEEE/ASME Int. Conf. Robot. Autom. (ICRA)*, Pasadena, CA, USA, May. 2008, pp. 419–424.
- [49] Q. Zhao, S. Liu, J. Chen, G. He, J. Di, L. Zhao, T. Su, M. Zhang, and Z. Hou, "Fast-moving piezoelectric micro-robotic fish with double caudal fins," *Robot. Auton. Syst.*, vol. 140, Jun. 2021, Art. no 103733.
- [50] K. Li, X. Zhou, Y. Liu, J. Sun, X. Tian, H. Zheng, . Zhang, J. Deng, J. Liu, W. Chen, and J. Zhao, "A 5 cm-scale piezoelectric jetting agile underwater robot," *Adv. Intell. Syst.*, vol. 5, no. 4, Apr. 2023, Art. no 2200262.
- [51] Y. S. Song and M. Sitti, "Surface-Tension-Driven Biologically Inspired Water Strider Robots: Theory and Experiments," *IEEE Trans. Robot.*, vol. 23, no. 3, pp. 578–589, Jun. 2007.
- [52] Y. Chen, N. Doshi, B. Goldberg, H. Wang, and R. J. Wood, "Controllable water surface to underwater transition through electrowetting in a hybrid terrestrial-aquatic microrobot," *Nature Commu.*, vol. 9, Jun. 2018, art. no. 2495.
- [53] X. Deng and S. Avadhanula, "Biomimetic Micro Underwater Vehicle with Oscillating Fin Propulsion: System Design and Force Measurement," in *Proc. IEEE/ASME Int. Conf. Robot. Autom. (ICRA)*, Barcelona, Spain, Apr. 2005, pp. 3312–3317.
- [54] A. Ming, S. Park, Y. Nagata, and M. Shimojo, "Development of Underwater Robots using Piezoelectric Fiber Composite," in *Proc. IEEE/ASME Int. Conf. Robot. Autom. (ICRA)*, Kobe, Japan, May 2009, pp. 3821–3826.
- [55] T. Fukuda, A. Kawamoto, F. Arai, and H. Matsuura, "Mechanism and Swimming Experiment of Micro Mobile Robot in Water," in *Proc. IEEE/ASME Int. Conf. Robot. Autom. (ICRA)*, San Diego, CA, USA, May 1994, pp. 814–819.
- [56] B. Kim, D.-H. Kim, J. Jung, and J.-O. Park, "A biomimetic undulatory tadpole robot using ionic polymer–metal composite actuators," *Smart Mater. Struct.*, vol. 14, no. 6, pp. 1579–1585, Dec. 2005.
- [57] N. Kamamichi, M. Yamakita, K. Asaka, and Z.-W. Luo, "A Snake-like Swimming Robot Using IPMC Actuator/Sensor," in *Proc. IEEE/ASME Int. Conf. Robot. Autom. (ICRA)*, Orlando, Florida, May 2006, pp. 1812–1817.
- [58] S. Guo, T. Fukuda, and K. Asaka, "A New Type of Fish-Like Underwater Microrobot," *IEEE/ASME Trans. Robot.*, vol. 8, no. 1, pp. 136–141, Mar. 2003.
- [59] E. M. Purcell, "Life at low Reynolds number," *Am. J. Phys.*, vol. 45, no. 1, pp. 3–11, Jan. 1977.
- [60] B. M. Finio, N. O. Pérez-Arancibia, and R. J. Wood, "System identification and linear time-invariant modeling of an insect-sized flapping-wing micro air vehicle," in *Proc. IEEE Int. Conf. Intell. Robots Syst. (IROS)*, San Francisco, CA, USA, Sep. 2011, pp. 1107–1114.